

Cellular Response to Proton Irradiation: A Simulation Study with TOPAS-nBio

Authors: Zhu, Hongyu, McNamara, Aimee L., McMahon, Stephen J., Ramos-Mendez, Jose, Henthorn, Nicholas T., et al.

Source: Radiation Research, 194(1) : 9-21

Published By: Radiation Research Society

URL: <https://doi.org/10.1667/RR15531.1>

BioOne Complete (complete.BioOne.org) is a full-text database of 200 subscribed and open-access titles in the biological, ecological, and environmental sciences published by nonprofit societies, associations, museums, institutions, and presses.

Your use of this PDF, the BioOne Complete website, and all posted and associated content indicates your acceptance of BioOne's Terms of Use, available at www.bioone.org/terms-of-use.

Usage of BioOne Complete content is strictly limited to personal, educational, and non - commercial use. Commercial inquiries or rights and permissions requests should be directed to the individual publisher as copyright holder.

BioOne sees sustainable scholarly publishing as an inherently collaborative enterprise connecting authors, nonprofit publishers, academic institutions, research libraries, and research funders in the common goal of maximizing access to critical research.

Cellular Response to Proton Irradiation: A Simulation Study with TOPAS-nBio

Hongyu Zhu,^{a,b,c} Aimee L. McNamara,^{a,d} Stephen J. McMahon,^e Jose Ramos-Mendez,^f Nicholas T. Henthorn,^g Bruce Faddegon,^f Kathryn D. Held,^{a,d} Joseph Perl,^h Junli Li,^{b,c} Harald Paganetti^{a,d} and Jan Schuemann^{a,d,1}

^a Department of Radiation Oncology, Massachusetts General Hospital, Boston, Massachusetts 02114; ^b Department of Engineering Physics, Tsinghua University, Beijing 100084, P.R. China; ^c Key Laboratory of Particle & Radiation Imaging (Tsinghua University), Ministry of Education, Beijing 100084, P.R. China; ^d Harvard Medical School, Boston, Massachusetts 02114; ^e Centre for Cancer Research and Cell Biology, Queens University Belfast, Belfast, United Kingdom; ^f Department of Radiation Oncology, University of California San Francisco, California 94143; ^g Division of Molecular and Clinical Cancer Sciences, Faculty of Biology, Medicine and Health, University of Manchester, Manchester, United Kingdom; and ^h SLAC National Accelerator Laboratory, Menlo Park, California

Zhu, H., McNamara, A. L., McMahon, S. J., Ramos-Mendez, J., Henthorn, N. T., Faddegon, B., Held, K. D., Perl, J., Li, J., Paganetti, H. and Schuemann, J. Cellular Response to Proton Irradiation: A Simulation Study with TOPAS-nBio. *Radiat. Res.* **194**, 9–21 (2020).

The cellular response to ionizing radiation continues to be of significant research interest in cancer radiotherapy, and DNA is recognized as the critical target for most of the biologic effects of radiation. Incident particles can cause initial DNA damages through physical and chemical interactions within a short time scale. Initial DNA damages can undergo repair via different pathways available at different stages of the cell cycle. The misrepair of DNA damage results in genomic rearrangement and causes mutations and chromosome aberrations, which are drivers of cell death. This work presents an integrated study of simulating cell response after proton irradiation with energies of 0.5–500 MeV (LET of 60–0.2 keV/μm). A model of a whole nucleus with fractal DNA geometry was implemented in TOPAS-nBio for initial DNA damage simulations. The default physics and chemistry models in TOPAS-nBio were used to describe interactions of primary particles, secondary particles, and radiolysis products within the nucleus. The initial DNA double-strand break (DSB) yield was found to increase from 6.5 DSB/Gy/Gbp at low-linear energy transfer (LET) of 0.2 keV/μm to 21.2 DSB/Gy/Gbp at high LET of 60 keV/μm. A mechanistic repair model was applied to predict the characteristics of DNA damage repair and dose response of chromosome aberrations. It was found that more than 95% of the DSBs are repaired within the first 24 h and the misrepaired DSB fraction increases rapidly with LET and reaches 15.8% at 60 keV/μm with an estimated chromosome aberration detection threshold of 3 Mbp. The dicentric and acentric fragment yields and the dose response of micronuclei formation after proton irradiation were calculated and

¹ Address for correspondence: Massachusetts General Hospital and Harvard Medical School, Radiation Oncology, Room 3206, 125 Nashua St., Boston, MA 02114; email: jschuemann@mgh.harvard.edu.

compared with experimental results. © 2020 by Radiation Research Society

INTRODUCTION

With the wide application of radiation therapy, the effect of ionizing radiation at the (sub-)cellular level has been the subject of substantial research. This is due to the strong evidence that DNA is the critical target for most of the biologic effects of radiation, including cell killing, carcinogenesis and mutation (1). Incident ionizing particles can induce DNA damage through the interaction of primary and secondary particles (direct) as well as through the interaction of radiolysis products with the DNA target volume (indirect) within a time scale of femtoseconds (10^{-15} s) to microseconds (10^{-6} s). DNA double-strand breaks (DSBs) are recognized as the most important lesions caused by radiation and can, for example, be experimentally investigated with pulsed-field gel electrophoresis (PFGE), single-cell gel electrophoresis (also known as the comet assay) and DNA damage-induced nuclear protein foci (radiation-induced foci assay) (1).

The initial DNA damages will undergo different repair pathways in the nucleus and can be repaired accurately, misrepaired or unrepaired (residual) after irradiation. The misrepaired and residual DSBs will lead to genomic rearrangements within or between chromosomes, resulting in different types of chromosome aberrations that can drive cell death. Chromosome aberrations can be experimentally measured by staining mitotic chromosomes with Giemsa or fluorescent probes (2).

Theoretically, DNA damage can be simulated with the Monte Carlo (MC) method using track structure simulations. Several Monte Carlo tools, e.g., PARTRAC (3), KURBUC (4), PITS (5), NASIC (6), RITRACKS (7, 8),

Geant4-DNA (9, 10), TOPAS-nBio (11) and GPU-based gMicroMC (12, 13), were developed to model physical, pre-chemical and chemical reactions in water, which can be regarded as a surrogate of biological tissue (14). The comprehensive track structure Monte Carlo code systems support simulation for photons, electrons, protons, neutrons and heavy ions (3, 9, 15). The combination of track structure simulations with nucleus geometry models is considered as the “gold standard” for predicting radiation-induced DNA damage spectrum (16). In addition to track structure Monte Carlo tools, the Monte Carlo damage simulation (MCDS) algorithm was developed for fast calculation of DNA lesions induced by various types of particles under different oxygen conditions (16–18). Such simulation tools are complementary to experimental studies, as they help interpret results and aid in generating hypotheses for further investigations.

To connect the initial DNA damage to chromosome aberrations, several *in silico* mechanistic DNA repair models were developed to describe the cellular processes related to DNA damage repair. The repair kinetics can be modeled with a set of differential equations or stochastic simulations. The biochemical kinetics model developed by Cucinotta *et al.* is one of the pioneering works that mathematically describes the binding of repair components (including Ku70/80, DNA-PKcs and the ligase IV-XRCC4 heterodimer) to DSBs with several intermediate repair complexes leading to DNA rejoining via the non-homologous end joining (NHEJ) pathway (19). Talei *et al.* proposed a mathematic kinetic model that considers more identified proteins involved in the NHEJ pathway (20, 21). Friedland *et al.* modeled the NHEJ repair pathway with stochastic simulation of attachment and dissociation of involved repair enzymes and step-by-step diffusion of DNA ends; this model was incorporated into PARTRAC and presented the first simulation framework for track structure, DNA damage, repair and chromosome aberration kinetics (22–24). The DNA Mechanistic Repair Simulator (DaMaRiS) framework (25, 26), developed at the University of Manchester, describes the scheme of the NHEJ pathway with stochastic simulation, and this model was applied to predict the dependence of DNA damage repair fidelity on damage density (26). This model was further modified by considering the homologous recombination (HR) pathway, and the results suggested an entwined relationship between the repair choice of NHEJ and HR (27). The Mechanistic DNA Repair and Survival (MEDRAS) model developed by McMahon *et al.* (28) is another milestone of mechanistic modeling of cellular radiation response. The MEDRAS model is based on temporal and spatial modeling of DNA repair incorporating a Gaussian spatial dependence of DSB misrejoining; it is the first single model that considers three key repair processes [NHEJ, HR and microhomology mediated end joining (MMEJ) pathways] with different repair fidelities and underlying mechanisms across the cell cycle in mammalian cells. MEDRAS is able to predict key

biological end points across a range of cell types, including repair kinetics, chromosome aberrations and cell survival. To facilitate cross-code comparison, both DaMaRiS and MEDRAS can read the standard DNA damage (SDD) data format (29), which is a standardized scoring method to link DNA damage induction simulations to the modeling of repair.

In this study, the cellular response after proton irradiation was investigated using track structure Monte Carlo simulations for damage induction and repair modeling with MEDRAS. A fibroblast nucleus model with a fractal geometry was built and implemented in TOPAS-nBio (11) for initial DNA damage yield simulations. The DNA damage yield results were scored in the SDD format and quantified by the yields of strand breaks (SBs), single-strand breaks (SSBs) and DSBs, and compared with published simulated and experimentally measured data. Furthermore, the dicentric and acentric fragment yields and micronuclei formation after proton irradiation were calculated and compared with experimental measurements by Edwards *et al.* (2), Wakatsuki *et al.* (30) and Yang *et al.* (31).

MATERIALS AND METHODS

DNA Model

A model of a human fibroblast nucleus at G₀/G₁ phase was built within the TOPAS-nBio framework. TOPAS-nBio is an extension to the TOPAS Monte Carlo application (32), which is based on Geant4 (33–35) to support simulation studies at the patient (macro and micro) scale (36, 37). The TOPAS-nBio extension is an advanced, yet user-friendly, Monte Carlo track structure simulation tool based on Geant4-DNA (9, 10). It offers an extensive library of advanced biological geometries ranging from the micrometer scale (e.g., cells and organelles) down to the nanometer scale (e.g., DNA molecules and proteins) (38) to support simulation studies at the cellular and sub-cellular levels with the goal of furthering our understanding of radiobiological effects at the DNA (nanometer) scale (38–40).

A full nucleus model was developed based on folding chromatin fibers in a fractal as indicated by Lieberman-Aiden *et al.* (41); the chromatin conformation is consistent with a knot-free fractal globule at the megabase scale. The fractal geometry of DNA was also adopted in other published work (42, 43). The DNA model was organized in a hierarchical structure including folding of the DNA double helix, nucleosomes, chromatin fibers and chromosomal territories.

DNA double helix. The DNA double helix (Fig. 1A) was formed with a half-cylindrical base volume with a radius of 0.5 nm and a quarter-cylindrical sugar-phosphate backbone volume with a radius of 1.15 nm based on the geometry in Henthorn *et al.* (44). The nucleotide pair has a height of 0.34 nm and was rotated by 36° for each subsequent pair. Additionally, a hydration shell with a thickness of 0.16 nm was built around the sugar-phosphate backbone. Ionizations within the shell can directly react with the DNA, causing direct DNA damage.

Nucleosome. The nucleosome (Fig. 1B) consists of a histone protein complex, modeled as a cylinder with a diameter of 6.6 nm and a length of 5.7 nm. The histone cylinder is wrapped with 1.65 left-handed turns (200 pairs of nucleotides) of the DNA double helix. The nucleosomes are connected to each other with 99 pairs of nucleotides, including linker DNA following a Bezier curve to ensure a smooth connection (44), forming a chromatin fiber.

Chromatin fiber, fiber loop and voxel. The chromatin fiber (Fig. 1C) has a radius of 37.1 nm and a length of 120 nm. The helix of

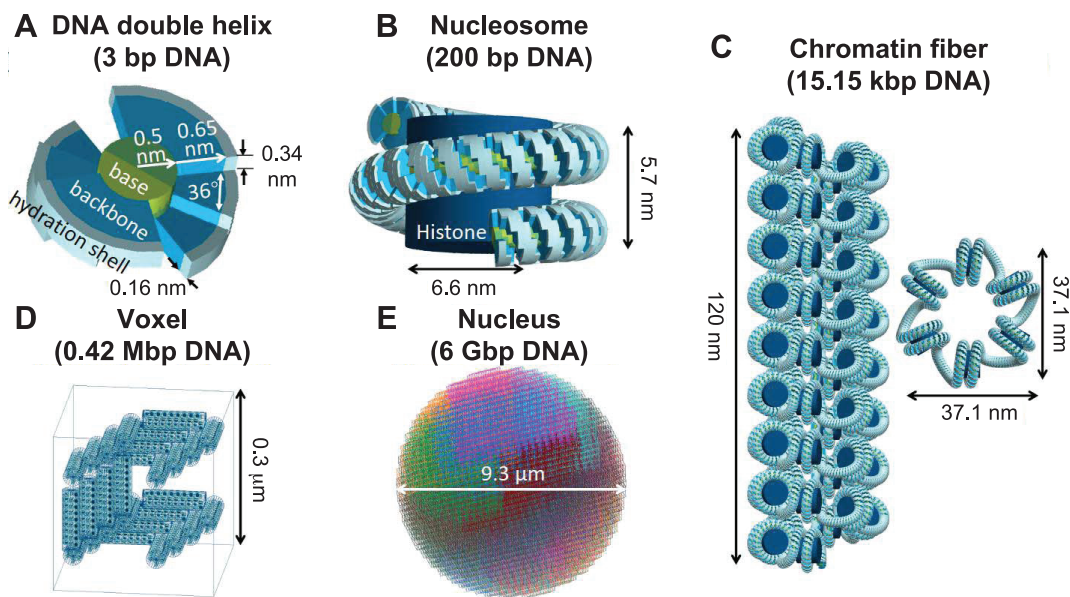


FIG. 1. Nuclear DNA model. Panel A: Double helix structure of the DNA model. Panel B: Structure of the nucleosome. Panel C: The chromatin fiber geometry. Panel D: A single voxel filled with four chromatin fiber loops, with each loop consisting of seven chromatin fibers folded in a fractal pattern. Panel E: The whole nucleus with 46 chromosomes. Voxels of the same color belong to the same chromosome, while different chromosomes are shown in different colors.

nucleosomes was built around the central axis of the fiber and set to repeat every six nucleosomes. Each fiber consists of 51 nucleosomes and contains 15,150 base pairs (bp) of DNA. Chromatin fibers were folded according to a continuous 3D Hilbert space-filling curve (38) to form chromatin fiber loops and fill a voxel (Fig. 1D). One chromatin fiber loop has seven chromatin fibers and was formed by a single iterated Hilbert curve, and four chromatin fiber loops were placed next to each other to use the space of the voxel efficiently. Each voxel has a side length of 0.3 μm and contains 0.42 Mbp of DNA.

Chromosomes and nucleus. The nucleus (Fig. 1E) has a spherical shape with a diameter of 9.3 μm and contains 46 chromosomes. The number of voxels and DNA content comprising each chromosome are summarized in Table 1. The full nucleus contains 14,328 voxels and 6.08 Gbp DNA, giving a final DNA density of 14.4 Mbp/ μm^3 , which is very close to the typical bp density of a mammalian nucleus (15 Mbp/ μm^3 (45)). The material of the nucleus is set to G4_WATER with a density of 1 g/ cm^3 , except for the backbone volume for which the density of G4_WATER is set to 1.407 g/ cm^3 (46) with cross sections scaled accordingly.

Simulation of Initial DNA Damage

The initial DNA damage after proton irradiation (0.5–500 MeV, corresponding to the LET region of 60–0.2 keV/ μm) was simulated with TOPAS-nBio (11). The nucleus model was placed at the center of a cubic world with a side length of 14 μm , large enough to contain the nucleus, which was filled with water with a density of 1 g/ cm^3 . To avoid a systematic alignment of proton tracks with the chromatin fiber, primary protons were initiated randomly on the surface of the nucleus and propagated inside the nucleus with a random direction. The induced DNA damage caused by direct and indirect interactions in the physical and chemical stages was quantified as either SBs, SSBs or DSBs (see below) and was output in the standard DNA damage (SDD) data format (29). To obtain sufficient statistics, 100 runs were performed for each energy point. Each simulation run had a fixed number of primaries and deposited a dose of 1 Gy within the nucleus. The statistical uncertainty of dose and DSB yield were smaller than 2%.

The track-length averaged LET was recorded as an index of radiation quality, and it was calculated with:

$$\text{LET} = \varepsilon/d, \quad (1)$$

where d is the mean proton cord length within the nucleus and ε is the energy deposition of all the primary and secondary particles within the nucleus.

Physical stage simulation. Direct DNA damage was induced from physical interactions between the primary and secondary particles within the DNA target. The recommended physics list of TOPAS-nBio for use in water radiolysis simulations (11) is contained in the physics module TsEmDNAPhysics. Most of the direct DNA damages after proton irradiation are caused by secondary electrons (>80%; see Appendix Fig. A1). The TsEmDNAPhysics module uses the following Geant4-DNA models to describe the interaction processes for electrons: G4DNAChampionElasticModel for elastic scattering processes (7.4 eV–1 MeV); G4DNABornExcitationModel for electronic excitation processes (9 eV–1 MeV); G4DNABornIonisationModel for ionization processes (11 eV–1 MeV); G4DNASancheExcitationModel for vibrational excitation processes (2 eV–100 eV); and G4DNAMeltonAttachmentModel for molecular attachment processes (4 eV–13 eV). The ionization cross section in the TsEmDNAPhysics module was extrapolated to support the simulation of protons up to 500 MeV while the default Geant4-DNA physics model (G4EmDNAPhysics) supports simulations of protons solely up to 100 MeV (9). TsEmDNAPhysics uses G4DNABornIonisationModel and cross-section data-adopted G4EmDNAPhysics for protons within 100 MeV and uses G4DNARuddIonisationExtendedModel and published cross-section data from RITRACKS (8) to support simulations of protons up to 500 MeV. Another advantage of the TsEmDNAPhysics module is that users can easily select the physics models of each interaction process with several command lines in the TOPAS-nBio parameter file.

Only interactions with the backbone led to DNA damage, i.e., base damage did not contribute to the recorded DNA damage. While interactions between primary and secondary particles on the backbone volumes were the main cause of direct SBs, it was assumed that

TABLE 1
Number of DNA Base Pairs and Voxels in Each Chromosome

Chromosome ID	Voxel Number	DNA base pairs (Mbp) ^a
1, 2	596	253
3, 4	585	248
5, 6	481	204
7, 8	461	196
9, 10	436	185
11, 12	412	175
13, 14	383	162
15, 16	352	149
17, 18	338	143
19, 20	326	138
21, 22	324	137
23, 24	319	135
25, 26	275	117
27, 28	256	109
29, 30	242	103
31, 32	214	91
33, 34	189	80
35, 36	183	78
37, 38	154	65
39, 40	150	64
41, 42	113	48
43, 44	119	50
Y	139	59
X	373	158
Total	14,328	6,078

^a Based on data from the Genome Reference Consortium (GRC) www.ncbi.nlm.nih.gov/grc. The nucleus contains 14,328 voxels and 6.08 Gbp DNA (1.02 times the reference data); therefore, the DNA content of each chromosome was scaled by a factor of 1.02 to assign voxels to chromosomes.

ionizations in the hydration shell could also lead to direct damage (47–49). A direct strand break (SB_{dir}) was formed if at least 17.5 eV of deposited energy was accumulated within the backbone volume and neighboring hydration shell within a single history.

Pre-chemical and chemical stage simulation. The TsEmDNA-Chemistry model (40) was used to simulate the chemical interactions in the pre-chemical stage and chemical stage. The TsEmDNAChemistry model inherited the capabilities to simulate water radiolysis of Geant4-DNA (50, 51), but used reviewed and updated chemistry parameters. These parameters included thermalization distance of solvated electron, diffusion coefficients and reaction rates in the G4EmDNAChemistry model. The TsEmDNAChemistry model was validated by calculating time-dependent G values (number of molecular species per 100 eV of energy deposited) for electrons, protons and α particles for a wide range of LET (0.05–230 keV/ μ m). All details have been provided elsewhere (40).

Following previous studies (43, 52–54), the chemical stage lasted up to 1 ns to mimic scavenging properties within the cell. To model the indirect DNA damages, all radiolysis products were simulated; however, only interactions between hydroxyl radicals (\cdot OH) and the DNA backbone were assumed to induce indirect strand breaks (SB_{indir}) with a reaction probability of 0.4 (42, 47). During the pre-chemical and chemical stage simulation, chemical species were created everywhere, because Geant4-DNA chemical processes consider only radiolysis of water. Then, the production of all chemical species in the DNA volumes (base, backbone, hydration shell and histone) were disregarded, i.e., the chemical molecules were terminated immediately if they were generated within the DNA volume. The DNA volumes were also regarded as a scavenger of hydroxyl (\cdot OH), solvated

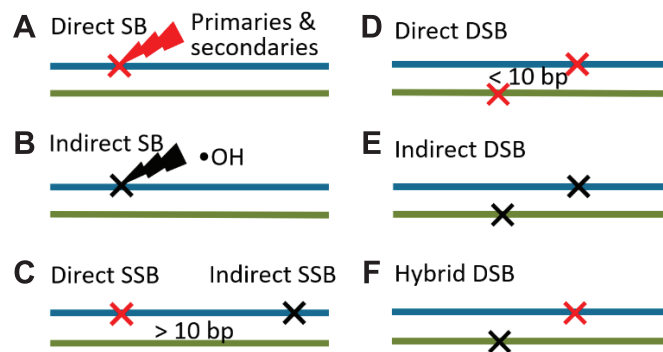


FIG. 2. DNA damage classification. Panel A: The formation of direct SBs was assumed to be caused by the interactions of primary and secondary particles in the DNA backbone volume and hydration shell during the physical stage of the simulation. Panel B: Indirect SBs were assumed to be induced by interactions between the hydroxyl radicals and the DNA backbone volume during the chemical simulation stage. Panel C: If two SBs were separated by more than 10 DNA base pairs then they are classified as SSBs, independent of whether they were on the same strand or on opposite strands. Panels D–F: If two SBs were located on the opposite side of DNA strands and separated by less than 10 base pairs, they are classified as a DSB.

electron (e_{aq}^-) and hydrogen (H^\bullet), i.e., these molecular species were scavenged if they diffused into the DNA volume.

Calculation of DSBs and SSBs. The initial SBs were categorized as DSBs and SSBs, as shown in Fig. 2. If two SBs were located on the opposite side of DNA strands and separated by less than 10 base pairs they were considered to cause a DSB; otherwise they were considered to be SSBs. DSBs were classified into three types: direct (two SBs both originated from direct interactions), indirect (two SBs both originated from indirect interactions) and hybrid (one SB originated from direct interaction while the other one originated from indirect interaction).

DNA Damage Repair and Micronuclei Formation

Mechanistic DNA repair model. The MEDRAS model developed by McMahon *et al.* (28) was used to describe the DNA damage repair process. Details about the model are described elsewhere (28, 55). The repair model considers NHEJ, HR and MMEJ repair processes within cells and has 11 parameters, including repair coefficients and fidelities of different repair processes, that were fitted with experimental data. The model aims at predicting key biological end points, including repair kinetics, chromosome aberrations and cell survival, among others, across a range of cell types. Recently, this model was updated by separating the DNA fragment end rejoining and foci clearance and refitted with additional datasets for more realistic description of DNA damage repair processes. The updated end rejoining coefficients of NHEJ (fast) and HR (slow) repair processes were $2.07 \pm 0.17/h$ and $0.26 \pm 0.01/h$, respectively. The newest version of the model is available as open source on GitHub: <https://github.com/sjcmahon/Medras-MC>.

The model starts from the initial DNA damages recorded in the SDD data format (29). Free DNA ends interact with other free DNA ends with a Gaussian separation-dependent probability (56):

$$\zeta(d) \propto e^{-\frac{d^2}{2\sigma^2}}, \quad (2)$$

where d is the separation between the two ends, σ is a characteristic rejoining range with a fitted value of $\sigma = 0.046R_{nuc}$, and R_{nuc} is the radius of the nucleus. The characteristic rejoining range ($\sim 0.21 \mu$ m) is relatively small compared to other models that focus on chromosome aberrations as a main end point [1 μ m or more (56, 57)]. This is

because the MEDRAS model considers all forms of misrepair, not only events that lead to chromosome aberrations, and many of these other types of misrepair occur over shorter ranges. The rejoining range in this case is in line with those of other models that focus on similar results [e.g., 70 nm (26) to 0.3 μm (58)]. For DSB breaks distributed uniformly within a spherical nucleus, the correct rejoin probability is:

$$P_{\text{correct}} = \frac{1 - e^{-\eta}}{\eta}, \quad (3)$$

where $\eta = \sum_{i=1}^{N-1} 2\zeta_i$ is the sum of the interaction rates between a free end in a given DSB with the remaining $N - 1$ DSBs (28). This expression is appropriate for low-LET irradiations such as X rays.

For the non-uniform damage distributions created by ions in this work, the misrejoin process was stochastically simulated by randomly sampling interactions between break ends, weighted according to the process-specific repair rates and the distance-dependent scaling in Eq. (2). This simulation considered all events until a given repair time, at which point DSB free ends may have been correctly repaired, misrepaired (misrejoin with free ends from other DSBs) or remained unrepaired.

Because DNA repair processes such as NHEJ do not have perfect fidelity, in addition to these binary misrepair events involving two DSBs, there is also a small chance of even isolated DSBs being incorrectly misrepaired. Previously published analytic models, in which this effect was quantified, obtained a fidelity of 98.54% for NHEJ, or equivalently a $1.46 \pm 0.2\%$ chance that such a break will be misrepaired (28). These additional misrepair events can then be added to the binary misrepair events to give the total yield of misrepair. This misrepair makes a negligible contribution at high doses and LETs, but is potentially more significant in low-dose low-LET regions.

Chromosome aberration. Each of the chromosomes had a centromere which was placed at the center of each chromosome in the MEDRAS model, i.e., if the chromosome had a length of 100 Mbp then the centromere was at the 50 Mbp position. One DSB splits the chromosome into two DNA fragments, one with a centromere and one without a centromere. The misrepair of DNA fragments leads to genomic rearrangements within or between chromosomes and may result in different types of chromosome aberrations, including dicentric (multi-centromere) and acentric (centromere free) fragments. In this study, the number of dicentric fragments (N_{DF}) and acentric fragments (N_{AF}) was counted after the repair process, based on the number of centromere(s) in the fragments after calculation of binary misrepair events. The impact of centromere position on the formation of acentric and dicentric fragments was investigated by modeling the placement of the centromere at different positions along the chromosome (10%, 30% and 50%). Our results show that the impact is less than 5% (data not shown).

Micronuclei (MN) mainly originate from acentric fragments or whole chromosomes that fail to be included in the daughter nuclei at the completion of telophase during mitosis and are correlated to cell killing (59–61). Experimentally, the formation of MN is usually scored in cytochalasin-blocked binucleated (BN) cells, which are cells attempting their first mitosis after irradiation. The percentage of BN cells with MN is usually used to describe the MN response to dose. The radiation dose response of BN cells with MN in the range 0–4 Gy is generally considered linear-quadratic for low-LET X rays and becomes linear for high-LET particles like protons and other heavy charged particles (59). MN can also be found in nonirradiated cells causing a background value of the percentage of BN cells with MN.

According to the origination of the MN, the number of MN can be analytically calculated with:

$$N_{MN} = p_1 N_{AF} + p_2 N_{WC}, \quad (4)$$

where, N_{AF} and N_{WC} are the number of acentric fragments and whole chromosomes, and p_1 and p_2 are the probability of acentric fragments and whole chromosomes that escape from the nucleus and form MN.

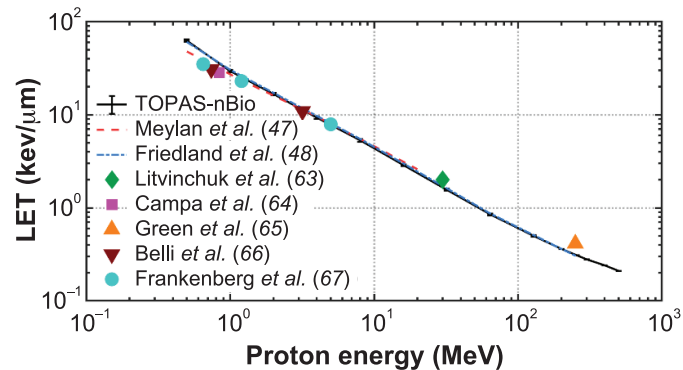


FIG. 3. Proton LET as a function of proton energy for simulation studies (lines) and experimental data (points) from Litvinchuk *et al.* (63), Campa *et al.* (64), Green *et al.* (65), Belli *et al.* (66) and Frankenberg *et al.* (67).

In this study, it was assumed that $N_{AF} = 0$ and $N_{WC} = 46$ for nonirradiated nuclei, i.e., only MN originating from whole chromosomes contribute to the background MN formation. Experimentally measured background MN levels vary over different studies (30, 31, 62). To better compare with experimental data, p_2 was set to 0 for irradiated nuclei and only MN originating from acentric fragments were considered. Predictions were compared to experimentally measured data after subtraction of background MN data.

Additional fragments resulting from the limited fidelity of NHEJ were incorporated in the calculation of MN yields after low-LET irradiation, where this contribution is expected to be relatively large. The formation of micronuclei was scored as the percentage of BN cells with MN, meaning that the number of cells with at least one MN was calculated. When cells are exposed to low-LET radiation at low dose, most of the initial DSBs can be correctly repaired and most of the cells may not contain any aberration (acentric, dicentric or MN); the number of BN cells with more than one MN can be underestimated if the repair fidelity of the NHEJ pathway is not considered, leading to significant difference with experimental data. The aberration yield per cell increases with LET as well as with dose, and the impact of repair fidelity gradually disappears when each cell has at least one MN on average. The number of additional acentric fragments can be empirically calculated with:

$$N_{AAF} = p_3 p_4 N_{DSB} D, \quad (5)$$

where N_{AAF} is the number of additional acentric fragments, $p_3 = 1.46 \pm 0.2\%$ is the base misrepair rate (28), and p_4 is the probability that one misrepair event leads to an acentric fragment above the chosen size threshold, for single-DSB misrepair events which are associated with the limited fidelity of NHEJ. N_{DSB} is the number of DSBs per nucleus per Gy, and D is the dose in the nucleus.

RESULTS AND DISCUSSION

Proton LET as a Function of Energy

Figure 3 shows the relationship between proton LET and particle energy simulated with TOPAS-nBio and digitalized from references. In low-energy regions, the discrepancy between different published data [maximum relative difference is 32.5% at 0.5 MeV between our calculation and Meylan *et al.* (47)] is mainly due to the size of the scoring volume, since low-energy protons probably cannot transverse the entire nucleus (e.g., the range of 0.5 MeV

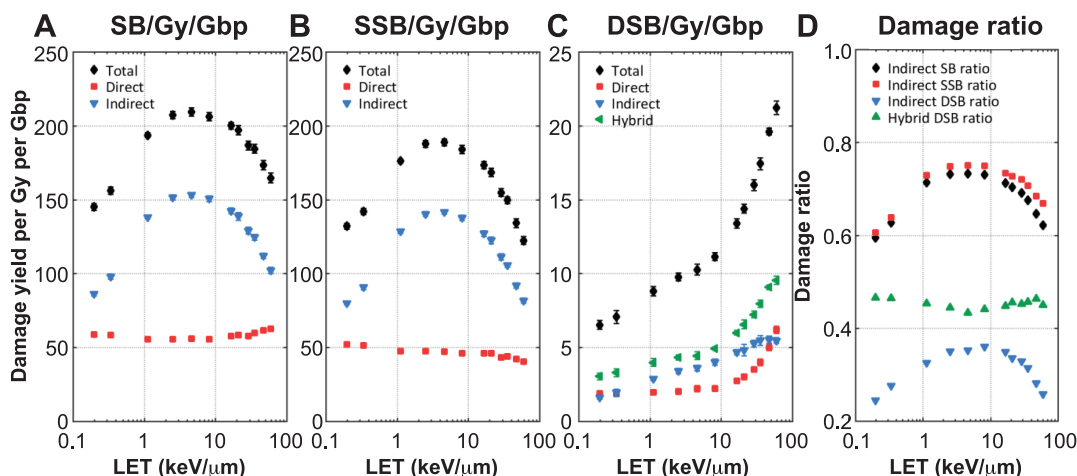


FIG. 4. The DNA damages obtained with TOPAS-nBio. Panel A: Total, direct and indirect SB yield per Gy per Gbp DNA. Panel B: Total, direct and indirect SSB yield per Gy per Gbp DNA. Panel C: Total, direct, indirect and hybrid DSB yield per Gy per Gbp DNA. Panel D: Contribution of indirect or hybrid damage to SB, SSB and DSB. Error bars represent standard errors and are mostly too small to be seen in the figure.

protons is $\sim 8.7 \mu\text{m}$ in liquid water). The impact of scoring volume on track-averaged LET was tested by scoring with the same nucleus geometry adopted by Meylan *et al.* (47) (an elliptical nucleus with a half axis of $2.5 \mu\text{m}$ along particle incident direction) and the relative difference was reduced to 2%. For the high-energy region ($>100 \text{ MeV}$), the LET values calculated with TOPAS-nBio agree by 4% with Friedland *et al.* (48).

Initial DNA Damage

Figure 4 shows the DNA damage results as a function of proton LET simulated with TOPAS-nBio. Simulated direct SB and SSB yields (Fig. 4A and B) are generally flat in the low-LET region. The direct SB yield slightly increases with LET in the higher LET region ($>10 \text{ keV}/\mu\text{m}$) and the direct SSB yield decreases slightly in high-LET regions because more SBs are categorized as DSBs. For indirect breaks, SB and SSB yields both initially increase with LET, before flattening at approximately $5 \text{ keV}/\mu\text{m}$ and then falling at higher LETs. For DSB damages (Fig. 4C), the direct DSB yield increases with the proton LET due to the denser local energy depositions of primary protons and secondary particles. The indirect DSB yield first increases with proton LET and then saturates at higher LET due to more chemical species being generated locally and interacting with each other, rather than with biological targets.

Figure 4D shows the relative contribution of indirect and hybrid damages as a fraction of each break type. Our simulations predicted that most of the SBs and SSBs would be caused by indirect damages and the indirect contribution ratio would increase from approximately 60% to approximately 75% at $4.5 \text{ keV}/\mu\text{m}$ (proton energy 10 MeV) and then decrease at higher LET where the production of radiolysis products becomes denser, thus leading to more chemical species interacting with each other rather than with

the DNA volume. Our simulations also showed that most of the DSB damages were classified as hybrid type, caused by the combined effect of direct and indirect damage.

Figure 5 shows the DNA damages obtained with TOPAS-nBio (black squares, dots, solid and dashed lines), compared to other simulated (42, 47–49, 53) or experimentally measured (64, 66–68) results. Our SB and SSB yields (Fig. 5A and B) agree well with previously published results by Friedland *et al.* (49) (blue diamonds) and show a consistent trend with the previous Geant4-DNA simulations (47) (magenta diamonds). To compare our DSB yield results (Fig. 5C) with other published data, short DNA fragments ($<10 \text{ kbp}$) were excluded, as they were assumed by others to be undetectable (42, 47, 48). The remaining DSBs are referred to as “distant DSBs” (49). The distant DSB yield increases with proton LET up to $30 \text{ keV}/\mu\text{m}$ and then decreases because more short DNA fragments are generated, due to the dense energy deposition distribution caused by high-LET protons, and then excluded. The ratio of SSB to DSB yield (Fig. 5D) obtained with TOPAS-nBio decreases with increasing LET, due to closer proximity of interaction events.

DNA Damage Repair

Figure 6 shows characteristics of DNA damage repair kinetics using the MEDRAS model (28, 55), after simulations of the physical and chemical stages. Figure 6A shows the residual DSB fraction as a function of repair time. It was predicted that more than 95% of the DSBs would be repaired within the first 24 h. The repair processes for DNA damages caused by high-LET protons are slower due to more complex damage (DSBs located close to each other) that are more difficult to repair. Figure 6B shows the predicted misrepair and residual DSB fractions after a 24-h repair process period as a function of the proton LET. The

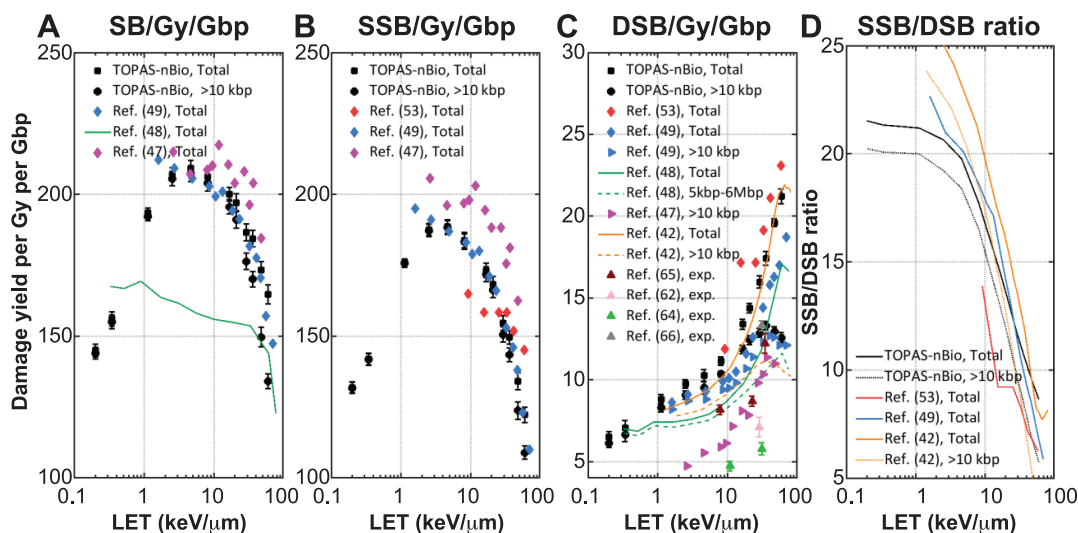


FIG. 5. Comparison of DNA damage obtained with TOPAS-nBio (black squares, dots, solid and dashed lines) and other simulated (diamonds, right triangles, solid and dashed lines) or experimentally measured data (up triangles). Panel A: SB yield per Gy per Gbp DNA. Panel B: SSB yield per Gy per Gbp DNA. Panel C: DSB yield per Gy per Gbp DNA. The experimental values measured by Frankenberg *et al.* (67), Campa *et al.* (64) and Belli *et al.* (66, 68) were generally measured using the PFGE method with different detection thresholds across different cell lines. Panel D: Ratio of SSB yield to DSB yield.

residual DSB fraction is initially flat ($\sim 1\%$) in low-LET regions and increases slightly at higher LETs, reaching up to 3.3% at 60.1 keV/μm (0.5 MeV proton). This delay in repair arises because rapid DSB repair requires other available free DSB ends within a relatively short separation. At high rates of misrepair, some DSB ends can become isolated and will take longer to rejoin with other distant DSB ends. For calculation of misrepair fractions, different DNA fragment detection thresholds were applied to exclude short DNA fragments for better quantification of misrepair fractions in experiments, since many assays are not sensitive to the tiny inversions or deletions caused by misrepair of

short DNA fragments. The predicted misrepair fractions increase rapidly with LET and reach 63.7% at 60.1 keV/μm without a fragment detection threshold. This value dropped to 15.8% with an estimated chromosome aberration detection threshold of 3 Mbp (69).

Chromosome Aberrations

The prediction of dicentric and acentric fragment yields in cells irradiated with 8.7 MeV protons and cultured 48 h postirradiation were compared with experimentally measured results in Fig. 7. It is important to note that a detection

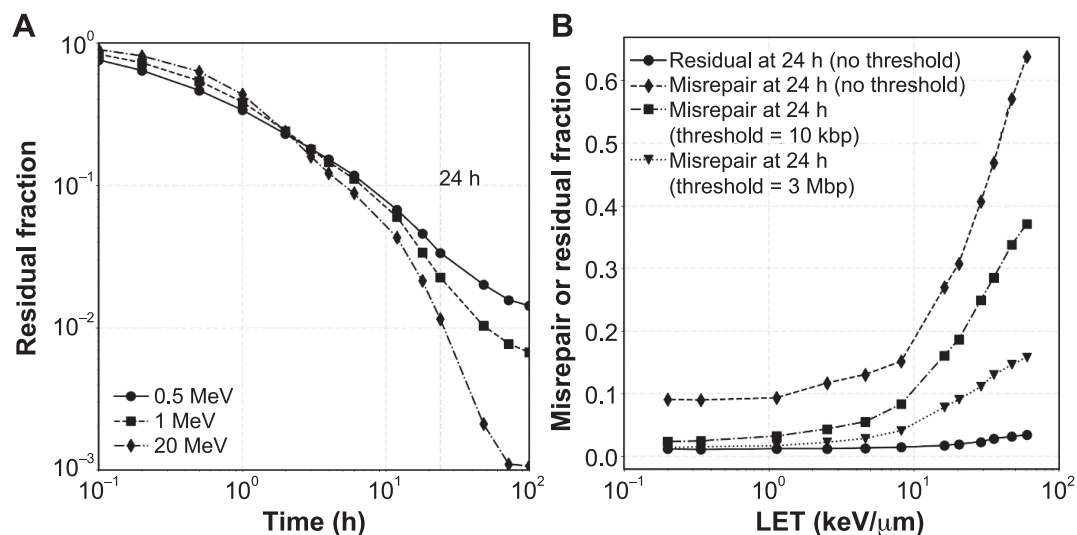


FIG. 6. Characteristics of DNA damage repair. Panel A: Residual DSB fractions as a function of repair time postirradiation with 0.5/1/20 MeV protons. Panel B: Misrepair or residual DSB fractions as a function of proton LET after 24 h of the repair process.

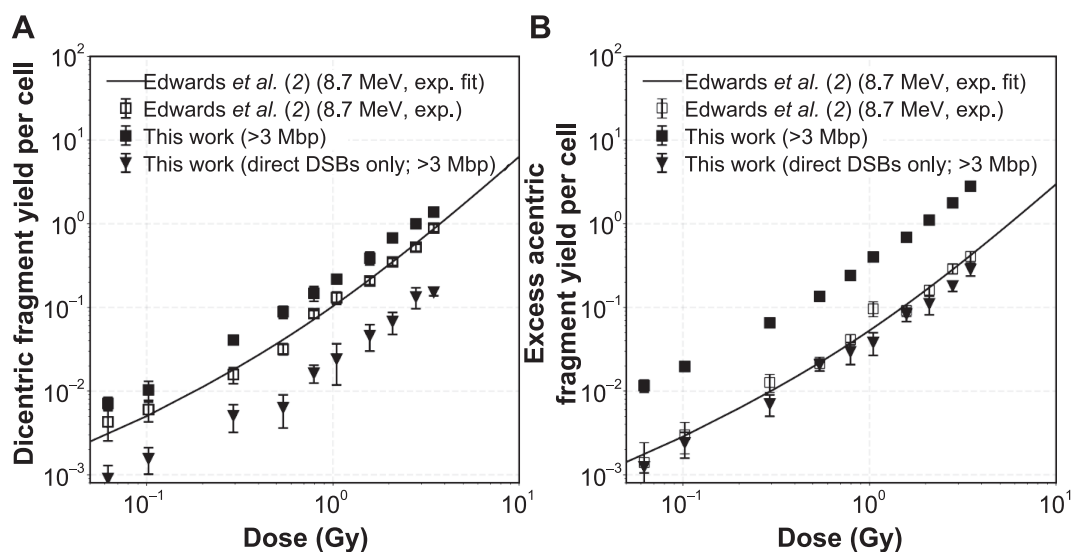


FIG. 7. Comparison of dicentric (panel A) and excess acentric (panel B) fragment yields in cells irradiated with 8.7 MeV protons and cultured 48 h postirradiation as a function of dose. Experimental data were extracted from Edwards *et al.* (2).

threshold of 3 Mbp was applied to calculate the number of detectable acentric fragments. Acentric fragments have a wide range of sizes, from tens of bp to Mbp, and many, particularly the smaller acentrics, may be undetectable. Acentric fragments in experiments were defined as excess acentric fragments, which were acentrics after allowing one for each dicentric fragment and centric ring (70). Therefore, the number of excess acentric fragments was calculated with the number of detectable acentric fragments subtracted by the number of dicentric fragments and the number of centric rings.

Predicted dicentric fragment yields (solid squares in Fig. 7A) and excess acentric fragment yields (solid squares in Fig. 7B) show a consistent quasi-linear trend with experimental data (open squares) throughout the investigated dose region, but with higher absolute values: dicentric fragment yields were overestimated by a factor of approximately 2 and excess acentric fragment yields were overestimated by a factor of approximately 10. There are a number of possible explanations for this: Experimental measurements can underestimate absolute values due to a detection threshold or resolution limitation, and the sensitivity of the Giemsa staining method ranges widely and depends on technical and examiner skill (71). Unlike dicentric fragments, acentric fragments have a wide range of sizes and many may be undetectable; this could lead to higher overestimation of excess acentric fragment yields than dicentric fragment yields.

Furthermore, TOPAS-nBio predicted a higher DSB yield than experimental results (Fig. 5C), which subsequently resulted in higher predicted chromosome aberration yields since the dicentric and acentric fragments originated from the misrepair of DSBs. The impact of DSB yields on chromosome aberration yields was quantified by calculating dicentric and excess acentric fragment yields with only

direct DSBs (which were $\sim 30\%$ of total DSBs, as shown in Fig. 4C), i.e., initial DNA damages were simulated with physics stage only. The resulting dicentric and excess acentric fragment yields (solid upside-down triangles in Fig. 7) were decreased by a factor of 10.

Additionally, the whole nucleus model as well as the repair model were both developed for fibroblasts, while experimental measurements were performed with lymphocytes, which are more prone to radiation-induced apoptosis (72, 73). In experiments, cells were assayed 48 h postirradiation, analyzing first division metaphases. Thus, cells that died in interphase (e.g., by apoptosis) or were arrested and had not reached mitosis would not be counted. Many of the large-sized acentric fragments are due to residual damages; cells, especially lymphocytes, with such damages may not make it to mitosis, leading to potentially significant differences in counts. In this work, the fibroblast nucleus model was used to represent lymphocytes as a simplifying assumption, while, actually, lymphocytes have different geometry characteristics. For instance, Friedland *et al.* developed different models for fibroblasts and lymphocytes (74). We have performed preliminary investigations (data not shown) of the impact of nucleus shape, and found that total rates of misrepair are not significantly affected until one dimension of the nucleus is very small ($< \sim 1 \mu\text{m}$), which is not the case for cell types considered here.

Figure 8 shows the comparison between predicted dose response of BN cells with MN and experimental data. The experiments were performed delivering 1 GeV protons with a reported LET of 0.2–0.24 keV/ μm . Our prediction was based on protons of 500 MeV (LET of 0.2 keV/ μm), which is the highest proton energy that can be simulated with the current TOPAS-nBio version. The probability (p_1) of acentric fragments that escape from the nucleus to form a MN was set to 0.5 (75). The predicted dose response of BN

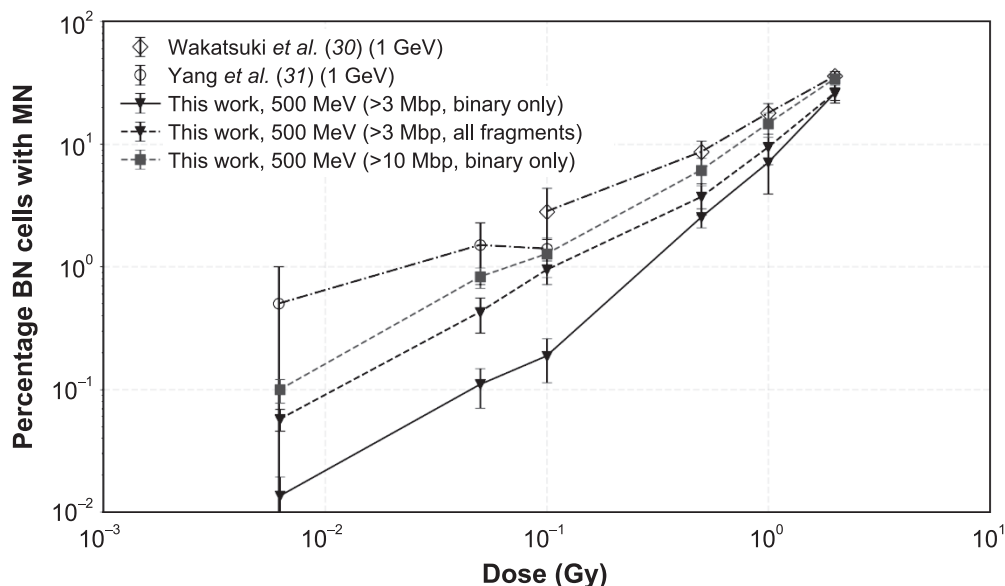


FIG. 8. Percentage of binucleated (BN) cells with micronuclei (MN) as a function of dose. The experimental data (30, 31) shown in the figure were net percentages (i.e., the background counts at 0 Gy irradiation were subtracted from measured values).

cells with MN with a detection threshold of 3 Mbp (solid triangles connected with solid line) generally shows a linear trend throughout the whole dose region, which is consistent with that indicated by Durante *et al.* (59). The predictions from the binary misrepair model are lower than experimental data, especially in the low-dose region. A potential reason for the lower predicted level in the lower dose region is that the experiments by Yang *et al.* (31) were performed at very low-dose levels (down to 6.25×10^{-8} Gy), where the MN response may be dominated by bystander signaling or the cells may fail to detect low levels of DNA damage and activate repair processes (76). Additionally, micronuclei may be more visible compared to acentric fragments, as they are wrapped in membrane; thus, the detection threshold for micronuclei may be lower.

Micronuclei yields from all acentric fragments, including binary misrepair and additional single-DSB misrepair, were considered with a detection threshold of 3 Mbp (solid triangles connected with dashed line in Fig. 8) and a lower detection threshold, 10 kbp (solid squares connected with dashed line in Fig. 8). For this work, p_4 was estimated to be 0.24 for acentric fragments larger than 3 Mbp and 0.41 for acentric fragments larger than 10 kbp after irradiation with 500 MeV protons. As shown, the dose response of BN cells with MN in the low-dose region was significantly corrected with a detection threshold of 10 kbp, agreeing within statistical uncertainties for all doses above 0.1 Gy (MN yield above 1%).

SUMMARY AND CONCLUSION

The cellular response after proton irradiation was studied by simulating the initial DNA damage in a whole nucleus

model with TOPAS-nBio and using the MEDRAS mechanistic repair model to predict the DNA damage repair processes and subsequent chromosome aberrations.

A whole nucleus model with a fractal DNA geometry, including the hierarchical structure of the genome from the DNA double helix, nucleosomes, chromatin fibers and chromosomal territories, was built and implemented in TOPAS-nBio. The spherical nucleus had a diameter of 9.3 μm and consisted of 46 chromosomes with a total DNA content and density of 6.08 Gbp and 14.4 Mbp/ μm^3 , respectively. The straight chromatin fibers and voxelized geometry used in this work were not as complex as the models developed in other published studies (15, 48). However, our simplified geometry significantly reduced the required computational memory and accelerated the navigation in Geant4 (as well as TOPAS); the initialization of the whole nucleus geometry can be finished within several minutes and a single simulation run with a 1 Gy dose in the nucleus generally can be completed within 10 h using a multi-thread (10 threads) mode [with Intel(R) Xeon(R) CPU L5640/X5660/E5450@2.27–3.00GHz]. In our current nucleus model the chromatin fibers were not smoothly connected. However, the impact of unlinked chromatin fibers should be negligible since the missing geometries are only a few base pairs every ~ 150 kbp.

The initial DNA damage yields induced by incident protons were simulated by modeling both the physical and chemical interactions within the nucleus with the default process models available in TOPAS-nBio. The initial SBs were found to be mostly caused by indirect damages (60–75%) and most of the DSBs were caused by the combined effect of direct and indirect damages. The total DSB yield increased from 6.5 DSB/Gy/Gbp in low-LET regions (0.2

keV/ μm) to 21.2 DSB/Gy/Gbp in the high-LET region (60.1 keV/ μm). With an increase in proton LET, more complex DNA damages and short DNA fragments were formed, with DSBs leading to detectable DNA fragments (>10 kbp) showing a saturation in the high-LET region.

By applying the mechanistic repair model, the characteristics of DNA damage repair and the dose response of chromosome aberrations were obtained. It was found that more than 95% of the DSBs are repaired within the first 24 h, and the highest misrepair fraction was 15.8% at 60 keV/ μm with an estimated chromosome aberration detection threshold of 3 Mbp. The number of chromosome aberrations after 48 h of repair time was also obtained and the predicted dicentric and excess acentric fragment yields shared consistent quasi-linear trends with experimental data, but with higher absolute values which can be attributed to the limitation of detection resolution in experiments, overestimation of initial damages and count loss due to experimental procedures. The dose responses of BN cells with MN were calculated and our results show that the non-zero misrepair rate has a significant impact on the predicted yield at low doses and LETs, and that a 10 kbp detection threshold may be more appropriate for predictions of micronuclei formation.

Our simulations show that Monte Carlo tools can predict DNA damage, and by incorporating a repair model, the DNA damage repair characteristics and chromosome aberration yields can be obtained. Such simulations can be employed to interpret experimental data and design new hypotheses. All simulations were done with the user-friendly framework of TOPAS-nBio, which does not require programming knowledge and has been made available as open-source code. Our results were recorded in the SDD data format, which facilitates inter-model comparisons, and can be easily used for related research benchmarks.

APPENDIX

Table A1 provides a summary of simulation setup, and Table A2 shows the damage yield (per Gy per Gbp) after proton (0.5–500 MeV) irradiation obtained using TOPAS-nBio. Figure A1 shows the energy deposition contribution in the DNA backbone and hydration shell from secondary electrons in the physics stage. Simulations were performed using the TsEmDNAPhysics model for different primary proton energies.

ACKNOWLEDGMENTS

HZ was sponsored by the China Scholarship Council for a year-long study abroad program at Massachusetts General Hospital. NH is supported by the European Union's Horizon 2020 Research and Innovation program under grant agreement no. 730983. This work was supported by the National Cancer Institute (grant no. R01 CA187003: TOPAS - nBio, a Monte Carlo Tool for Radiation Biology Research). Simulations were performed on the O2 High Performance Compute Cluster, supported by the Research Computing Group at Harvard Medical School, and the ERISOne cluster, supported by Partners Information Services at Partners Healthcare Systems.

Received: September 30, 2019; accepted: April 11, 2020; published online: May 13, 2020

REFERENCES

- Hall EJ, Giaccia AJ. Radiobiology for the radiologist. 8th ed. Philadelphia, PA: Lippincott Williams & Wilkins; 2018.
- Edwards AA, Lloyd DC, Prosser JS, Finnon P, Moquet JE. Chromosome aberrations induced in human lymphocytes by 8.7 MeV protons and 23.5 MeV helium-3 ions. *Int J Radiat Biol Relat Stud Phys Chem Med* 1985; 50:137–45.
- Friedland W, Dingfelder M, Kundrat P, Jacob P. Track structures, DNA targets and radiation effects in the biophysical Monte Carlo simulation code PARTRAC. *Mutat Res* 2011; 711:28–40.
- Uehara S, Nikjoo H, Goodhead D. Cross-sections for water vapour for the Monte Carlo electron track structure code from 10 eV to the MeV region. *Phys Med Biol* 1993; 38, 1841.
- Wilson W, Nikjoo H. A Monte Carlo code for positive ion track simulation. *Radiat Environ Biophys* 1999; 38:97–104.
- Li J, Li C, Qiu R, Yan C, Xie W, Wu Z, et al. DNA strand breaks induced by electrons simulated with Nanodosimetry Monte Carlo Simulation Code: NASIC. *Radiat Prot Dosimetry* 2015; 166:38–43.
- Plante I, Devroye L. Considerations for the independent reaction times and step-by-step methods for radiation chemistry simulations. *Radiat Phys Chem* 2017; 139:157–72.
- Plante I, Cucinotta FA. Ionization and excitation cross sections for the interaction of HZE particles in liquid water and application to Monte Carlo simulation of radiation tracks. *New J Phys* 2008; 10:125020.
- Bernal MA, Bordage MC, Brown JMC, Davidkova M, Delage E, El Bitar Z, et al. Track structure modeling in liquid water: A review of the Geant4-DNA very low energy extension of the Geant4 Monte Carlo simulation toolkit. *Phys Med* 2015; 31:861–74.
- Incerti S, Baldacchino G, Bernal M, Capra R, Champion C, Francis Z, et al. The Geant4-DNA Project. *International Journal of Modeling, Simulation, and Scientific Computing* 2010; 01:157–78.
- Schuemann J, McNamara AL, Ramos-Mendez J, Perl J, Held KD, Paganetti H, et al. TOPAS-nBio: An extension to the TOPAS Simulation Toolkit for cellular and sub-cellular radiobiology. *Radiat Res* 2019; 191:125–38.
- Tsai MY, Tian Z, Qin N, Yan C, Lai Y, Hung SH, et al. A new open-source GPU-based microscopic Monte Carlo simulation tool for the calculations of DNA damages caused by ionizing radiation—Part I: Core algorithm and validation. *Med Phys* 2020; 47:1958–70.
- Lai Y, Tsai MY, Tian Z, Qin N, Yan C, Hung SH, et al. A new open-source GPU-based microscopic Monte Carlo simulation tool for the calculations of DNA damages caused by ionizing radiation — Part II: Sensitivity and uncertainty analysis. *Med Phys* 2020; 47:1971–82.
- Nikjoo H, Uehara S, Emfietzoglou D, Cucinotta FA. Track-structure codes in radiation research. *Radiat Meas* 2006; 41:1052–74.
- Nikjoo H, Emfietzoglou D, Liamsuwan T, Taleei R, Liljequist D, Uehara S. Radiation track, DNA damage and response—a review. *Rep Prog Phys* 2016; 79:116601.
- Semenenko V, Stewart R. A fast Monte Carlo algorithm to simulate the spectrum of DNA damages formed by ionizing radiation. *Radiat Res* 2004; 161, 451–7.
- Stewart RD, Yu VK, Georgakilas AG, Koumenis C, Park JH, Carlson DJ. Effects of radiation quality and oxygen on clustered DNA lesions and cell death. *Radiat Res* 2011; 176:587–602.
- Semenenko V, Stewart R. Fast Monte Carlo simulation of DNA damage formed by electrons and light ions. *Phys Med Biol* 2006; 51:1693.
- Cucinotta FA, Pluth JM, Anderson JA, Harper JV, O'Neill P. Biochemical kinetics model of DSB repair and induction of gamma-H2AX foci by non-homologous end joining. *Radiat Res* 2008; 169:214–22.

20. Taleei R, Girard PM, Nikjoo H. DSB repair model for mammalian cells in early S and G1 phases of the cell cycle: Application to damage induced by ionizing radiation of different quality. *Mutat Res Genet Toxicol Environ Mutagen* 2015; 779:5–14.
21. Taleei R, Nikjoo H. The non-homologous end-joining (NHEJ) pathway for the repair of DNA double-strand breaks: I. A mathematical model. *Radiat Res* 2013; 179:530–9.
22. Friedland W, Jacob P, Kundrat P. Mechanistic simulation of radiation damage to DNA and its repair: on the track towards systems radiation biology modelling. *Radiat Prot Dosimetry* 2010; 143:542–8.
23. Friedland W, Jacob P, Kundrat P. Stochastic simulation of DNA double-strand break repair by non-homologous end joining based on track structure calculations. *Radiat Res* 2010; 173:677–88.
24. Friedland W, Kundrat P. Track structure based modelling of chromosome aberrations after photon and alpha-particle irradiation. *Mutat Res Genet Toxicol Environ Mutagen* 2013; 756:213–23.
25. Warmenhoven JW, Henthorn NT, Ingram SP, Chadwick AL, Sotiropoulos M, Korabel N, et al. Insights into the non-homologous end joining pathway and double strand break end mobility provided by mechanistic in silico modelling. *DNA Repair* 2020; 85:102743.
26. Henthorn NT, Warmenhoven JW, Sotiropoulos M, Mackay RI, Kirkby NF, Kirkby KJ, et al. In silico non-homologous end joining following ion induced DNA double strand breaks predicts that repair fidelity depends on break density. *Sci Rep* 2018; 8:2654.
27. Ingram SP, Warmenhoven JW, Henthorn NT, Smith EAK, Chadwick AL, Burnet NG, et al. Mechanistic modelling supports entwined rather than exclusively competitive DNA double-strand break repair pathway. *Sci Rep* 2019; 9:6359.
28. McMahon SJ, Schuemann J, Paganetti H, Prise KM. Mechanistic modelling of DNA repair and cellular survival following radiation-induced DNA damage. *Sci Rep* 2016; 6:33290.
29. Schuemann J, McNamara AL, Warmenhoven JW, Henthorn NT, Kirkby KJ, Merchant MJ, et al. A new standard DNA damage (SDD) data format. *Radiat Res* 2019; 191:76–92.
30. Wakatsuki M, Magpayo N, Kawamura H, Held KD. Differential bystander signaling between radioresistant chondrosarcoma cells and fibroblasts after X-ray, proton, iron ion and carbon ion exposures. *Int J Radiat Oncol Biol Phys* 2012; 84:e103–8.
31. Yang H, Magpayo N, Rusek A, Chiang IH, Sivertz M, Held KD. Effects of very low fluences of high-energy protons or iron ions on irradiated and bystander cells. *Radiat Res* 2011; 176:695–705.
32. Perl J, Shin J, Schumann J, Faddegon B, Paganetti H. TOPAS: An innovative proton Monte Carlo platform for research and clinical applications. *Med Phys* 2012; 39:6818–37.
33. Agostinelli S, Allison J, Amako K, Apostolakis J, Araujo H, Arce P, et al. GEANT4: A simulation toolkit. *Nucl Instrum Meth A* 2003; 506:250–303.
34. Allison J, Amako K, Apostolakis J, Araujo H, Dubois PA, Asai M, et al. Geant4 developments and applications. *IEEE Trans Nucl Sci* 2006; 53:270–8.
35. Allison J, Amako K, Apostolakis J, Arce P, Asai M, Aso T, et al. Recent developments in Geant4. *Nucl Instrum Methods Phys Res A* 2016; 835:186–225.
36. Verburg JM, Grassberger C, Dowdell S, Schuemann J, Seco J, Paganetti H. Automated Monte Carlo simulation of proton therapy treatment plans. *Technol Cancer Res Treat* 2016; 15:NP35–NP46.
37. Schumann J, Paganetti H, Shin J, Faddegon B, Perl J. Efficient voxel navigation for proton therapy dose calculation in TOPAS and Geant4. *Phys Med Biol* 2012; 57:3281–93.
38. McNamara AL, Ramos-Mendez J, Perl J, Held K, Dominguez N, Moreno E, et al. Geometrical structures for radiation biology research as implemented in the TOPAS-nBio toolkit. *Phys Med Biol* 2018; 63:175018.
39. McNamara A, Geng C, Turner R, Mendez JR, Perl J, Held K, et al. Validation of the radiobiology toolkit TOPAS-nBio in simple DNA geometries. *Phys Med* 2017; 33:207–15.
40. Ramos-Mendez J, Perl J, Schuemann J, McNamara A, Paganetti H, Faddegon B. Monte Carlo simulation of chemistry following radiolysis with TOPAS-nBio. *Phys Med Biol* 2018; 63:105014.
41. Lieberman-Aiden E, Van Berkum NL, Williams L, Imakaev M, Ragoczy T, Telling A, et al. Comprehensive mapping of long-range interactions reveals folding principles of the human genome. *Science* 2009; 326:289–93.
42. Sakata D, Lampe N, Karamitros M, Kyriakou I, Belov O, Bernal MA, et al. Evaluation of early radiation DNA damage in a fractal cell nucleus model using Geant4-DNA. *Phys Med* 2019; 62:152–7.
43. Lampe N, Karamitros M, Breton V, Brown JMC, Sakata D, Sarramia D, et al. Mechanistic DNA damage simulations in Geant4-DNA Part 2: Electron and proton damage in a bacterial cell. *Phys Med* 2018; 48:146–55.
44. Henthorn NT, Warmenhoven JW, Sotiropoulos M, Mackay RI, Kirkby KJ, Merchant MJ. Nanodosimetric simulation of direct ion-induced DNA damage using different chromatin geometry models. *Radiat Res* 2017; 188:690–703.
45. Ghosh SK, Jost D. How epigenome drives chromatin folding and dynamics, insights from efficient coarse-grained models of chromosomes. *PLoS Comput Biol* 2018; 14:e1006159.
46. Smialek MA, Jones NC, Hoffmann SV, Mason NJ. Measuring the density of DNA films using ultraviolet-visible interferometry. *Phys Rev E Stat Nonlin Soft Matter Phys* 2013; 87:060701.
47. Meylan S, Incerti S, Karamitros M, Tang N, Bueno M, Clairand I, et al. Simulation of early DNA damage after the irradiation of a fibroblast cell nucleus using Geant4-DNA. *Sci Rep* 2017; 7:11923.
48. Friedland W, Schmitt E, Kundrat P, Dingfelder M, Baiocco G, Barbieri S, et al. Comprehensive track-structure based evaluation of DNA damage by light ions from radiotherapy-relevant energies down to stopping. *Sci Rep* 2017; 7:45161.
49. Friedland W, Jacob P, Bernhardt P, Paretzke HG, Dingfelder M. Simulation of DNA damage after proton irradiation. *Radiat Res* 2003; 159:401–10.
50. Karamitros M, Mantero A, Incerti S. Modeling radiation chemistry in the Geant4 toolkit. *Prog Nucl Sci Technol* 2011; 2:503–8.
51. Karamitros M, Luan S, Bernal MA, Allison J, Baldacchino G, Davidkova M, et al. Diffusion-controlled reactions modeling in Geant4-DNA. *J Comput Phys* 2014; 274:841–2.
52. Mokari M, Alamatsaz MH, Moeini H, Taleei R. A simulation approach for determining the spectrum of DNA damage induced by protons. *Phys Med Biol* 2018; 63:175003.
53. Nikjoo H, O'Neill P, Wilson W, Goodhead D. Computational approach for determining the spectrum of DNA damage induced by ionizing radiation. *Radiat Res* 2001; 156:577–83.
54. Watanabe R, Rahmanian S, Nikjoo H. Spectrum of radiation-induced clustered non-DSB damage – A Monte Carlo track structure modeling and calculations. *Radiat Res* 2015; 183:525–40.
55. McMahon SJ, McNamara AL, Schuemann J, Paganetti H, Prise KM. A general mechanistic model enables predictions of the biological effectiveness of different qualities of radiation. *Sci Rep* 2017; 7:10790.
56. Ponomarev AL, George K, Cucinotta FA. Computational model of chromosome aberration yield induced by high- and low-LET radiation exposures. *Radiat Res* 2012; 177:727–37.
57. Ballarini F, Altieri S, Bortolussi S, Carante M, Giroletti E, Protti N. The BIANCA model/code of radiation-induced cell death: application to human cells exposed to different radiation types. *Radiat Environ Biophys* 2014; 53:525–33.
58. Friedrich T, Durante M, Scholz M. Modeling cell survival after photon irradiation based on double-strand break clustering in megabase pair chromatin loops. *Radiat Res* 2012; 178:385–94.
59. Durante M, Formenti SC. Radiation-induced chromosomal

- aberrations and immunotherapy: Micronuclei, cytosolic DNA, and interferon-production pathway. *Front Oncol* 2018; 8:192.
60. Luzhna L, Kathiria P, Kovalchuk O. Micronuclei in genotoxicity assessment: from genetics to epigenetics and beyond. *Front Genet* 2013; 4:131.
 61. Fenech M, Kirsch-Volders M, Natarajan AT, Surrallés J, Crott JW, Parry J, et al. Molecular mechanisms of micronucleus, nucleoplasmic bridge and nuclear bud formation in mammalian and human cells. *Mutagenesis* 2011; 26:125–32.
 62. Miszczyk J, Rawojc K, Panek A, Swakon J, Prasanna PG, Rydygier M. Response of human lymphocytes to proton radiation of 60 MeV compared to 250 kV X-rays by the cytokinesis-block micronucleus assay. *Radiother Oncol* 2015; 115:128–34.
 63. Litvinchuk AV, Vachelova J, Michaelidesova A, Wagner R, Davidkova M. Dose-dependent micronuclei formation in normal human fibroblasts exposed to proton radiation. *Radiat Environ Biophys* 2015; 54:327–34.
 64. Campa A, Ballarini F, Belli M, Cherubini R, Dini V, Esposito G, et al. DNA DSB induced in human cells by charged particles and gamma rays: experimental results and theoretical approaches. *Int J Radiat Biol* 2005; 81:841–54.
 65. Green LM, Murray DK, Tran DT, Bant AM, Kazarians G, Moyers MF, et al. Response of thyroid follicular cells to gamma irradiation compared to proton irradiation. I. Initial characterization of DNA damage, micronucleus formation, apoptosis, cell survival, and cell cycle phase redistribution. *Radiat Res* 2001; 155:32–42.
 66. Belli M, Cherubini R, Dalla Vecchia M, Dini V, Moschini G, Signoretti C, et al. DNA DSB induction and rejoining in V79 cells irradiated with light ions: a constant field gel electrophoresis study. *Int J Radiat Biol* 2000; 76:1095–104.
 67. Frankenberg D, Brede HJ, Schrewe UJ, Steinmetz C, Frankenberg-Schwager M, Kasten G, et al. Induction of DNA double-strand breaks by 1 H and 4 He Ions in primary human skin fibroblasts in the LET range of 8 to 124 keV/mm. *Radiat Res* 1999; 151:540–9.
 68. Belli M, Cherubini R, Dalla Vecchia M, Dini V, Esposito G, Moschini G, et al. DNA fragmentation in mammalian cells exposed to various light ions. *Adv Space Res* 2001; 27:393–9.
 69. Cornforth MN, Bedford JS. A quantitative comparison of potentially lethal damage repair and the rejoining of interphase chromosome breaks in low passage normal human fibroblasts. *Radiat Res* 1987; 111:385–405.
 70. Edwards AA, Lloyd DC, Purrott RJ. Radiation induced chromosome aberrations and the Poisson distribution. *Radiat Environ Biophys* 1979; 16:89–100.
 71. Long SS, Prober CG, Fischer M. Principles and practice of pediatric infectious diseases. 5th ed. Philadelphia, PA: Elsevier; 2018.
 72. Hendry JH, West CM. Apoptosis and mitotic cell death: their relative contributions to normal-tissue and tumour radiation response. *Int J Radiat Biol* 1997; 71:709–19.
 73. Ross GM. Induction of cell death by radiotherapy. *Endocr Relat Cancer* 1999; 6:41–44.
 74. Friedland W, Paretzke HG, Ballarini F, Ottolenghi A, Kreth G, Cremer C. First steps towards systems radiation biology studies concerned with DNA and chromosome structure within living cells. *Radiat Environ Biophys* 2008; 47:49–61.
 75. Savage JRK. A comment on the quantitative relationship between micronuclei and chromosomal aberrations. *Mutat Res Lett* 1988; 207:33–6.
 76. Rothkamm K, Lobrich M. Evidence for a lack of DNA double-strand break repair in human cells exposed to very low X-ray doses. *Proc Natl Acad Sci U S A* 2003; 100:5057–62.

TABLE A1
Summary of Simulation Setup

Simulation tool	TOPAS-nBio
Source	0.5–500 MeV protons. Randomly sampled on the surface of the nucleus, pointing inside the nucleus with a random direction
Number of histories	1,000–250,000 primaries (depending on proton energy)
Simulation time	<10 h to finish a run with a dose of 1 Gy within the nucleus [10 threads mode on Intel(R) Xeon(R) CPU L5640/X5660/E5450@2.27–3.00GHz]
Statistical uncertainty	DNA damage yield uncertainty <2%
Geometry	Spherical fibroblast nucleus in G ₁ /G ₀ phase, 9.3 μm in diameter, water, density = 1 g/cm ³ (except backbone density = 1.4 g/cm ³)
Physics and chemistry model	TsEmDNAPhysics, TsEmDNAChemistry (1 ns chemical stage)
Induction of direct SB	>17.5 eV energy deposition in the backbone and neighboring hydration shell
Induction of indirect SB	Assuming only ·OH can cause indirect damage with a probability of 0.4
Induction of DSB	2 SB on opposite strands of DNA, located within 10 base pairs

TABLE A2
Damage Yield (per Gy per Gbp) after Proton (0.5–500 MeV) Irradiation Obtained with TOPAS-nBio

Energy (MeV)	LET (keV/ μm)	Total SB	Direct SB	Indirect SB	Total SSB	Direct SSB	Indirect SSB	Total DSB	Direct DSB	Indirect DSB	Hybrid DSB
0.5	60.09	134.07	47.90	86.17	108.91	35.29	73.62	21.21	6.20	5.46	9.55
0.6	47.62	149.68	50.73	98.95	123.76	38.41	85.35	19.60	5.00	5.52	9.07
0.8	35.77	170.06	53.74	116.33	143.46	41.75	101.71	17.42	3.99	5.47	7.96
1	29.18	176.34	53.39	122.95	150.61	42.08	108.53	15.98	3.50	5.25	7.23
1.5	20.95	191.15	56.02	135.13	166.31	45.26	121.04	14.37	3.00	4.82	6.55
2	16.72	195.57	55.82	139.75	171.87	45.72	126.14	13.39	2.74	4.66	5.99
5	8.20	204.01	54.62	149.39	183.31	46.00	137.31	11.14	2.22	4.01	4.91
10	4.64	207.33	55.18	152.15	188.28	47.05	141.22	10.25	2.21	3.60	4.44
20	2.53	205.36	54.96	150.40	187.23	47.23	140.00	9.76	2.02	3.41	4.33
50	1.13	192.27	54.84	137.44	175.69	47.48	128.21	8.80	1.95	2.86	3.98
200	0.34	155.02	57.71	97.31	141.73	51.20	90.53	7.07	1.84	1.95	3.28
500	0.20	143.96	58.31	85.65	131.72	51.92	79.80	6.52	1.89	1.59	3.04

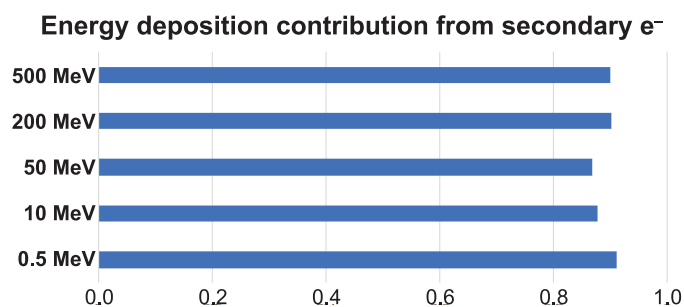


FIG. A1. Energy deposition contribution in the DNA backbone and hydration shell from secondary electrons in the physics stage. Simulations were performed using the TsEmDNAPhysics model for different primary proton energies.